Flood Inundation Area Prediction under Climate Change Scenarios by Integrating Hydrological and Hydraulic Models with a Hybrid Deep Learning Framework

Tongchana Nawasanchai , Piyapong Tongdeenok * , Naruemol Kaewjampa

Posted Date: 30 March 2026

doi: 10.20944/preprints202603.2381.v1

Keywords: flood inundation modeling; low-gradient monsoon floodplains; hydrological–hydraulic coupling; hybrid deep learning; climate change projection

 doi:10.20944/preprints202603.2381.v1

Article

Flood Inundation Area Prediction Under Climate Change Scenarios by Integrating Hydrological and Hydraulic Models with a Hybrid Deep Learning Framework

Tongchana Nawasanchai, Piyapong Tongdeenok * and Naruemol Kaewjampa

Watershed Management Program, Department of Conservation, Faculty of Forestry, Kasetsart University, Bangkok 10900, Thailand

* Correspondence: piyapong@ku.th or fforppt@ku.ac.th

Abstract

Flood inundation modelling in low-gradient monsoon floodplains requires a physically consistent representation of rainfall–runoff–inundation processes. This study develops a hybrid modelling framework that integrates a coupled hydrological–hydraulic model (HEC-HMS–HEC-RAS) with a deep learning–based LSTM–U-Net surrogate to represent temporal hydrological memory and spatial inundation patterns. The framework is applied to the Upper Songkhram River Basin in northeastern Thailand, a storage-dominated floodplain strongly influenced by monsoon hydrology. The hydrological model demonstrated strong validation performance (NSE = 0.896, KGE = 0.827, R^2 = 0.909), while hydraulic simulations showed high spatial agreement with satellite-derived inundation maps (F1 = 0.876, Kappa = 0.873). Trained on hydraulically simulated discharge–inundation pairs, the LSTM–U-Net model successfully reproduced two-dimensional flood patterns across independent flood events (mean F1 = 0.838, IoU = 0.721), with prediction errors mainly occurring along shallow floodplain margins. Future projections under CMIP6 SSP2-4.5 and SSP5-8.5 indicate substantial increases in flood-season discharge (up to ~80%), whereas maximum inundation extent expands more moderately (≤21%), reflecting nonlinear floodplain response in low-gradient systems. The proposed framework preserves hydrological–hydraulic consistency while supporting future flood inundation projection, climate-informed flood risk assessment, and adaptation planning.

Keywords: flood inundation modeling; low-gradient monsoon floodplains; hydrological–hydraulic coupling; hybrid deep learning; climate change projection

1. Introduction

Flooding is a major natural hazard in monsoon-dominated regions, where prolonged rainfall often causes extensive inundation across low-gradient floodplains [1]. Increasing flood frequency and severity have been linked to climate change-driven intensification of the hydrological cycle and shifts in precipitation extremes [1,2]. In storage-dominated basins, even moderate changes in seasonal discharge can substantially affect floodplain activation [3]. This reflects the important role of floodplain storage and channel–floodplain interactions, which can limit the proportional expansion of inundation extent [4–6].

Physically based hydrological–hydraulic models provide a process-based representation of flood generation, from rainfall and runoff to floodplain inundation [7]. Hydrological models simulate rainfall–runoff processes and river discharge, but they generally cannot resolve the spatial dynamics of floodplain inundation [7]. In contrast, hydraulic models explicitly represent water surface elevation, river routing, and two-dimensional floodplain flow processes [8], but they require discharge hydrographs as upstream boundary conditions [9]. Therefore, integrating models such as

 doi:10.20944/preprints202603.2381.v1

HEC-HMS and HEC-RAS enables physically consistent simulation of flood processes through a one-way coupling framework that transfers hydrological forcing to floodplain inundation [10]. However, representing floodplain response under multiple future scenarios remains challenging, especially in low-gradient systems where inundation depends on both hydrological forcing and spatial floodplain processes [11].

Deep learning has increasingly been used as a surrogate for hydraulic simulations because it can capture complex nonlinear relationships and spatiotemporal flood behavior [12–15]. However, many existing approaches rely on static or event-based predictors [13,14] and do not explicitly account for hydrological memory, which is especially important in storage-influenced floodplains [4,11,16]. Antecedent hydrological conditions can strongly affect flood magnitude and duration [11,16,17], highlighting the need to include temporal state dynamics in flood modelling. As a result, generalization across different flood magnitudes under changing climate conditions remains difficult [18,19]. A methodological gap therefore remains in developing surrogate models that can represent both temporal hydrological memory and spatial inundation response while preserving physical causality [17,20–22].

To address this gap, this study develops a physics-constrained hybrid framework that integrates a Long Short-Term Memory (LSTM)-based temporal encoder with a spatial decoding network, forming a hybrid deep learning surrogate of the hydraulic model. Trained strictly on hydraulically simulated inundation states, the model explicitly captures antecedent discharge dynamics while remaining embedded within a consistent climate–hydrology–hydraulics sequence. The framework is applied to the Upper Songkhram River Basin in northeastern Thailand to evaluate performance across contrasting flood magnitudes and to assess projected inundation changes under SSP2-4.5 and SSP5-8.5 scenarios [18,23].

2. Materials and Methods

2.1. Study Area

The study was conducted in the Upper Songkhram River Basin, located in Ban Muang District, Sakon Nakhon Province, northeastern Thailand (Figure 1). The basin forms part of the Songkhram River system, a major tributary of the Mekong River [24], and represents a flood-prone lowland catchment that is highly sensitive to monsoon-driven hydrological variability.

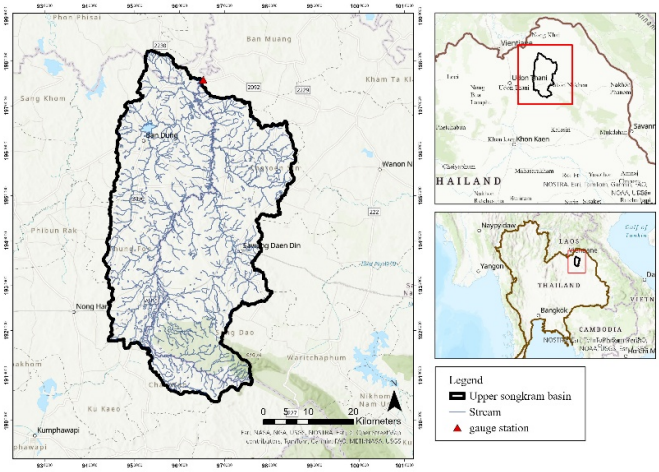

Figure 1. Location of the Upper Songkhram River Basin and the study area.

Topographically, the basin shows a clear upstream-downstream gradient, with headwaters originating from the Phu Phan Mountain range and downstream areas forming a wide low-lying floodplain (Figure 2). The elevation and slope maps derived from the 12.5 m ALOS PALSAR DEM

 doi:10.20944/preprints202603.2381.v1

[25] indicate predominantly gentle terrain (~1-3%), which limits drainage efficiency and promotes widespread floodplain inundation during high-flow conditions.

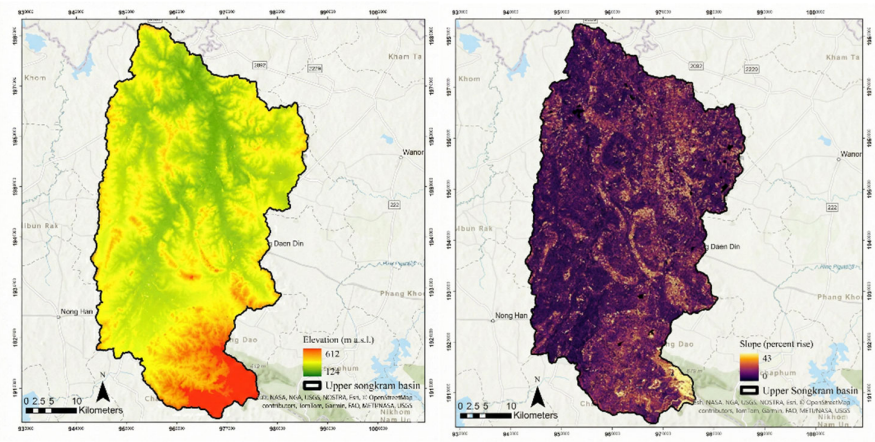

(**a**) (**b**)

Figure 2. Topographic characteristics of the study area: elevation (a) and slope (b).

The floodplain adjacent to the main river channel extends approximately 1-3 km on both sides and functions as a natural floodwater storage zone [26]. Combined with the basin's low relief and gentle slope, this setting promotes widespread lateral inundation during high-flow conditions [3]. Key physical and geomorphological characteristics of the basin are summarized in Table 1.

Table 1. Physical and geomorphological characteristics of the Upper Songkhram River Basin.

Category	Value	Unit
Basin area	2,174.65	km²
Basin perimeter	415.40	km
Maximum elevation	619	m a.s.l.
Minimum elevation	124	m a.s.l.
Mean elevation	183.32	m a.s.l.
Mean basin slope	2.21	%
Floodplain width	1–3	km
Main channel length	116.67	km
Basin shape	Elongated (rectangular)	–
Drainage pattern	Dendritic	–

Hydrologically, the Upper Songkhram River Basin is dominated by the Southwest Monsoon, with most annual rainfall occurring between July and October, frequently producing seasonal riverine flooding over the low-lying floodplain [27]. The basin has experienced several severe flood events in recent decades, including a major flood in 2017 that caused widespread inundation [28], indicating high sensitivity to extreme hydrological conditions [23]. Owing to its low-gradient floodplain morphology and seasonally persistent discharge regime, the basin provides a suitable case for flood inundation modelling under both historical and future climate conditions.

2.2. Overview of the Hybrid Modeling Framework

This study proposes a hybrid flood inundation modeling framework (Figure 3) that couples a physically based hydrological–hydraulic modeling system with a deep learning–based LSTM–U-Net flood inundation model. Hydrological simulations using HEC-HMS generate river discharge, which is applied as upstream forcing to a two-dimensional HEC-RAS model to produce spatial flood inundation maps. The resulting discharge–inundation datasets under historical conditions are used to train and validate a deep learning model that emulates hydraulic flood patterns from antecedent discharge conditions. Climate change scenarios are introduced only during the prediction stage,

 doi:10.20944/preprints202603.2381.v1

ensuring that the deep learning model functions strictly as a surrogate of the hydraulic model rather than as part of the climate forcing chain.

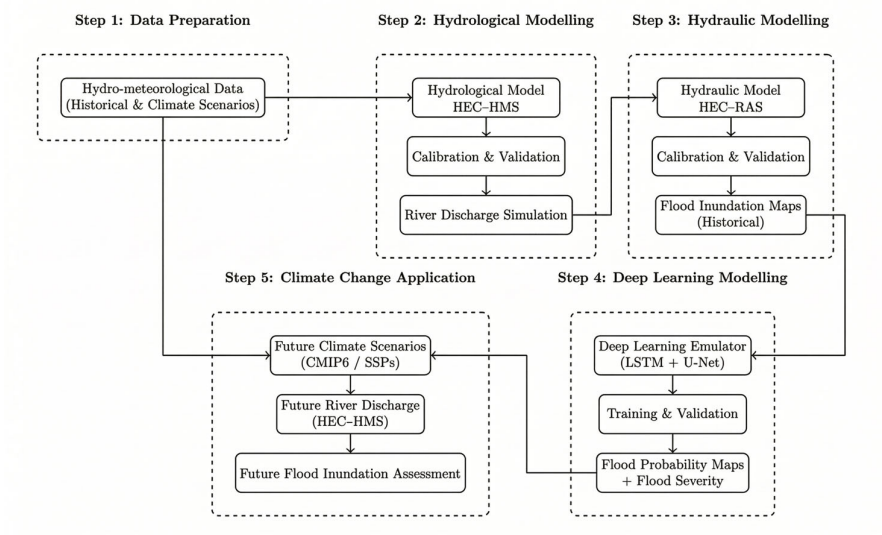

Figure 3. Conceptual framework of the coupled hydrological–hydraulic and deep learning modelling system.

2.3. Hydrological Modeling Using HEC-HMS

2.3.1. Model Configuration and Purpose

Hydrological processes in the study basin were simulated using HEC-HMS to generate daily discharge time series at the basin outlet (KH.74 gauging station), which were used as upstream boundary conditions for the hydraulic model. The model was run at a daily time step and calibrated using observed streamflow data for 2012-2020, with validation for 2021-2024. Standard runoff generation, baseflow, and routing components available in HEC-HMS were applied following common flood-oriented hydrological modeling practice [29,30].

2.3.2. Hydrological Process Representation and Flow Routing

Runoff generation was simulated using the Soil Conservation Service Curve Number (SCS-CN) method, which estimates direct runoff as a nonlinear function of rainfall, land use, soil properties, and antecedent moisture conditions [31,32]. Based on the watershed storage concept, surface runoff is assumed to occur only after initial abstraction is satisfied, with the curve number (CN) parameter representing the combined effects of soil and land cover. Direct runoff Q is computed from rainfall P as

$$Q = \begin{cases} 0, & P \le I_a \\ \dfrac{(P - I_a)^2}{P - I_a + S}, & P > I_a \end{cases} \quad (1)$$

where I_a represents initial abstraction and S is the potential maximum retention.

Excess rainfall was transformed into direct runoff hydrographs using the Snyder unit hydrograph method, which relates hydrograph shape and timing to basin geometry and drainage characteristics [33,34]. Baseflow contribution was represented using the recession method, assuming exponential decay of groundwater discharge following storm events [30,34]. Channel routing was performed using the Muskingum method, which represents channel storage as a weighted function of inflow and outflow and is widely applied to simulate flood wave propagation in river channels [35].

 doi:10.20944/preprints202603.2381.v1

2.4. Hydraulic Modeling Using HEC-RAS

2.4.1. Governing Equations

Floodplain hydraulics were simulated using the two-dimensional (2D) HEC-RAS module, which solves the depth-averaged shallow water (Saint-Venant) equations for unsteady flow over complex terrain [36,37]. The governing equations comprise the continuity and momentum equations in the x and y directions. The continuity equation is:

$$\frac{\partial h}{\partial t} + \frac{\partial (hu)}{\partial x} + \frac{\partial (hv)}{\partial y} = 0 \quad (2)$$

and the momentum equations in the x and y directions are:

$$\frac{\partial (hu)}{\partial t} + \frac{\partial (hu^2)}{\partial x} + \frac{\partial (huv)}{\partial y} = -g\,h\frac{\partial z}{\partial x} - g\,h\,S_{fx} \quad (3)$$

$$\frac{\partial (hv)}{\partial t} + \frac{\partial (huv)}{\partial x} + \frac{\partial (hv^2)}{\partial y} = -g\,h\frac{\partial z}{\partial y} - g\,h\,S_{fy} \quad (4)$$

where h is water depth, u and v are depth-averaged velocity components, z is bed elevation, and S_f is the friction slope computed using Manning's equation [36].

2.4.2. Flood Inundation Simulation Using HEC-RAS

The two-dimensional HEC-RAS model computes spatially distributed water depth and velocity fields, from which inundation extent is delineated based on positive water depth [37]. Flood maps were exported as raster datasets representing channel–floodplain interactions and were used as reference data for training and evaluating the LSTM–U-Net model. HEC-RAS has been widely applied for high-resolution flood hazard assessment [37–39].

The model was implemented using a computational mesh derived from the ALOS PALSAR DEM (12.5 m resolution) with a grid size of 50 m. Manning's roughness coefficients were assigned based on land use characteristics. Upstream discharge simulated by HEC-HMS was applied as boundary forcing, while downstream conditions were specified using normal depth. Simulations were performed under unsteady flow conditions with a 12 h time step to ensure numerical stability while remaining consistent with the daily resolution of the input data.

2.5. Deep Learning-Based Flood Inundation

The deep learning model is designed as a computational surrogate of the physically based hydraulic model (Figure 4), rather than an independent flood prediction system. The model learns the nonlinear relationship between antecedent river discharge and spatial inundation patterns simulated by the two-dimensional HEC-RAS model [40]. It produces flood probability maps using a sigmoid activation function to generate pixel-wise inundation probabilities.

As the model is trained exclusively on hydraulically simulated flood maps, it preserves consistency with the hydrological–hydraulic modelling framework while enabling efficient large-scale floodplain analysis. Model training used hydraulically simulated discharge–inundation pairs from four representative flood years (2013, 2017, 2018, and 2023), while two independent flood years (2019 and 2024) were reserved for validation to assess event-level generalization.

 doi:10.20944/preprints202603.2381.v1

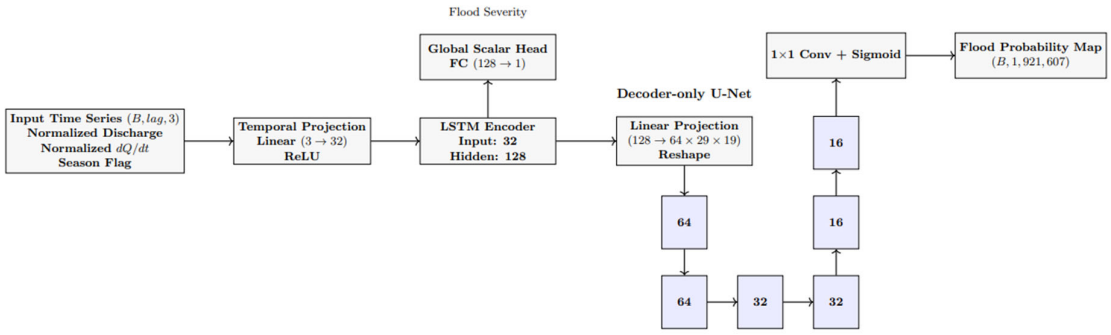

Figure 4. Structure of the hybrid deep learning flood inundation model.

2.5.1. Temporal Encoding and Latent Representation

The deep learning model receives lagged hydrological sequences derived from discharge simulations. Each time step includes three normalized inputs: river discharge, its first-order temporal derivative (dQ/dt), and a binary seasonal indicator representing wet-season conditions. These variables are used to characterize antecedent hydrological conditions that influence floodplain activation. Based on preliminary sensitivity analysis (T = 2, 5, 8, 10, and 15), a lag length of T = 10 was selected due to superior validation performance.

The input sequence is processed by a Long Short-Term Memory (LSTM) network [41] to capture temporal dependencies and hydrological memory effects. The final hidden state is then transformed into a latent spatial representation, which serves as the interface between temporal encoding and subsequent spatial reconstruction in the flood emulation framework [14].

2.5.2. U-Net–Inspired Spatial Decoding

Flood inundation patterns are reconstructed using a decoder-only U-Net-inspired architecture [42]. Unlike the original U-Net, the proposed model does not include a symmetric convolutional encoder or skip connections; instead, it operates on the latent spatial representation generated by the temporal encoder.

The decoder progressively upsamples the latent representation through a sequence of convolutional blocks to recover the spatial structure of the floodplain. A final convolution layer with sigmoid activation produces a flood inundation probability map, in which each grid cell represents the predicted probability of inundation.

2.5.3. Multi-Task Learning and Model Evaluation

To improve representation learning, the model includes an auxiliary flood severity head operating on the shared LSTM hidden state. Flood severity is defined as the fraction of inundated area within the spatial domain and is predicted through a fully connected layer.

A multi-task learning framework is adopted to jointly optimize spatial flood prediction and severity estimation [43]. The total loss function is defined as

$$L = L_{flood} + \lambda L_{severity} \quad (5)$$

where L_{flood} is a weighted combination of binary cross-entropy loss and Dice loss to address class imbalance between flooded and non-flooded pixels [44], and $L_{severity}$ is defined as mean squared error. Joint optimization encourages the shared temporal encoder to learn hydrologically meaningful latent representations that improve generalization across flood events of varying magnitudes.

 doi:10.20944/preprints202603.2381.v1

2.6. Climate Data and Future Precipitation Projections

2.6.1. Climate Model Data and Model Selection

Future precipitation projections were obtained from twelve CMIP6 Global Climate Models (GCMs) using daily precipitation archives [18]. To address coarse spatial resolution and systematic biases in raw GCM outputs, empirical quantile mapping (QM) was applied using the historical reference period (1994-2014), and the derived bias correction was subsequently applied to future projections [45]. The corrected precipitation data were downscaled to a spatial resolution of approximately 2.5 km and formatted for compatibility with the hydrological modeling framework.

Model performance during the historical period was evaluated using Taylor diagrams, considering correlation coefficient (R), root mean square error (RMSE), and standard deviation [46]. Among the evaluated models, IITM-ESM demonstrated the highest overall skill and was therefore selected for subsequent projection analysis. Future projections were analyzed under two CMIP6 Shared Socioeconomic Pathways, SSP2-4.5 and SSP5-8.5, representing intermediate and high-emission scenarios, respectively, with the bias correction consistently applied.

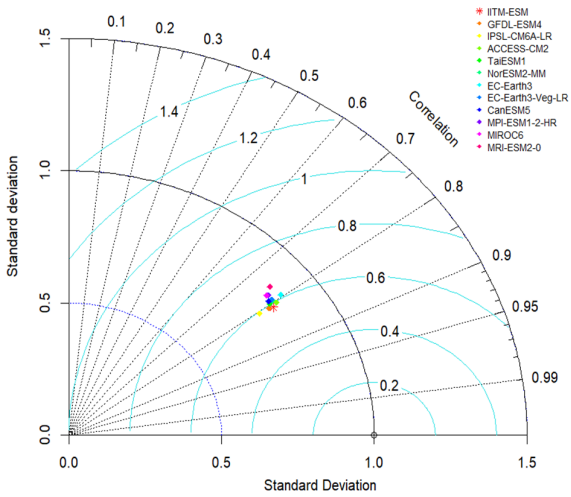

Figure 5. Taylor diagram of CMIP6 GCM performance used for model selection based on historical precipitation (1994–2014).

2.7. Evaluation Metrics

2.7.1. Hydrological Performance Metrics

Hydrological model performance was evaluated by comparing observed and simulated daily discharge using Nash-Sutcliffe efficiency (NSE), Kling-Gupta efficiency (KGE), coefficient of determination (R^2), and root mean square error (RMSE) [47–49]. NSE and KGE assess overall agreement in magnitude, variability, and temporal dynamics, while R^2 and RMSE quantify linear association and error magnitude, respectively. The NSE and KGE formulations are given by:

The Nash–Sutcliffe efficiency is defined as

$$NSE = 1 - \frac{\sum_{t=1}^{T}\left(Q_t^{obs} - Q_t^{sim}\right)^2}{\sum_{t=1}^{T}\left(Q_t^{obs} - \overline{Q^{obs}}\right)^2} \quad (6)$$

where $\boldsymbol{Q_t^{obs}}$ and $\boldsymbol{Q_t^{sim}}$ denote the observed and simulated discharge at time step t, respectively, $\overline{\boldsymbol{Q^{obs}}}$ is the mean observed discharge, and T is the total number of time steps. NSE values closer to unity indicate better model performance [47].

 doi:10.20944/preprints202603.2381.v1

2.7.2. Flood Inundation Spatial Performance Metrics

Spatial performance of flood inundation simulations and deep learning predictions was evaluated through pixel-wise comparison between reference and modeled flood maps. Inundation maps were converted to binary classes, and classification-based metrics including Precision, Recall, F1-score, Intersection over Union (IoU), and Kappa coefficient were computed [50–52]. These metrics are widely used for spatial evaluation of flood inundation models.

The F1-score was adopted as the primary indicator of spatial prediction performance, as it balances omission and commission errors. The F1-score, Intersection over Union (IoU) and Kappa formulations are defined as: The F1-score is defined as

$$F1=\frac{2TP}{2TP+FP+FN} \quad (7)$$

where TP, FP, and FN denote the number of true positives, false positives, and false negatives, respectively.

3. Results

3.1. Performance of the Coupled Hydrological–Hydraulic Model

The hydrological component was calibrated for the period 2012–2020 and validated for 2021–2024 at the KH.74 streamflow gauging station in the Upper Songkhram River Basin. Figure 6 shows good agreement between observed and simulated daily discharge, with the HEC-HMS model accurately capturing seasonal dynamics and major flood peaks. Quantitative evaluation yielded an NSE of 0.896, KGE of 0.827, R^2 of 0.909, and RMSE of 18.13 m^3/s, indicating high predictive skill in reproducing daily discharge variability and peak flows.

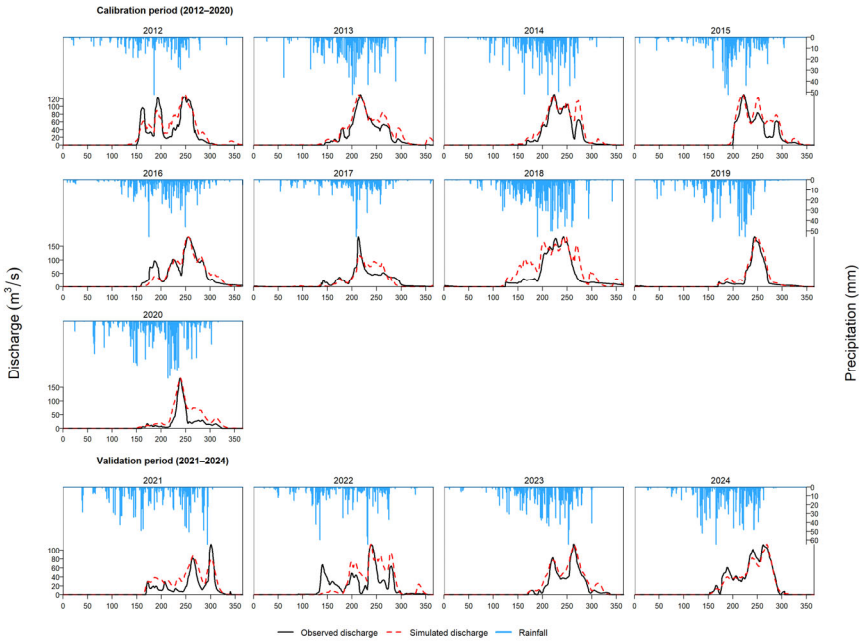

Figure 6. Performance of the HEC-HMS model in simulating daily streamflow during the calibration (2012–2020) and validation (2021–2024) periods.

The hydraulic model was evaluated by comparing simulated flood extents with satellite-derived inundation maps from GISTDA for three major flood years (2017, 2023, and 2024). Annual maximum flood extents were extracted and aggregated for assessment. The results indicate strong spatial agreement, with an overall F1-score of 0.876 and Kappa of 0.873, while precision and recall (Table 2)

 doi:10.20944/preprints202603.2381.v1

confirm accurate delineation of flooded areas. The simulated mean annual maximum inundation area (74.93 km²) closely matches the observed extent (77.02 km²), corresponding to a relative difference of 2.7%.

Table 2. Spatial performance of HEC-RAS flood inundation maps compared with observed flood extent.

Year	Precision	Recall	F1-score	Kappa
2017	0.875	0.903	0.889	0.885
2023	0.885	0.858	0.871	0.869
2024	0.910	0.817	0.861	0.858

3.2. Performance Evaluation of the LSTM–U-Net Model

3.2.1. Effect of Lag Length on Model Performance

To evaluate the influence of temporal memory on the LSTM encoder, different lag lengths (T = 2, 5, 8, 10, and 15 days) were tested, and model performance was assessed using F1-score, IoU, and Kappa (Figure 7). Model performance improved as the lag length increased from 2 to 10 days, and the best performance was obtained at T = 10, which produced the highest F1, IoU, and Kappa values among the tested configurations.

Short lag lengths (T = 2–5) resulted in lower accuracy, while an excessively long lag (T = 15) caused a substantial decrease in performance. Based on these results, a lag length of 10 days was selected for all subsequent experiments.

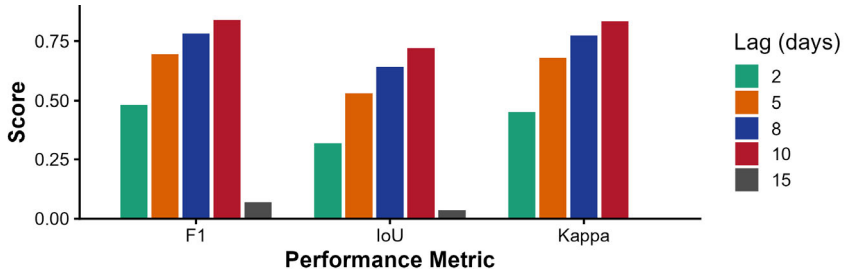

Figure 7. Sensitivity of model performance to lag length for the LSTM–U-Net.

3.2.2. Spatial Performance of the LSTM–U-Net Model

The results indicate strong spatial agreement between predicted and reference inundation maps (mean F1 = 0.838, IoU = 0.721, Kappa = 0.833; Table 3), reflecting substantial spatial overlap and balanced classification performance across independent validation events.

Table 3. Spatial performance of the LSTM-U-Net model.

Event	IoU	F1-score	Kappa
2019	0.703	0.826	0.819
2024	0.729	0.843	0.838
Mean	0.721	0.838	0.833

3.2.3. Event-Based Validation and Error Characteristics

The spatial behavior of the LSTM–U-Net model was further evaluated using stage-specific flood maps from the 2019 and 2024 validation events, with corresponding quantitative metrics summarized in Table 4. Across all stages, the model maintains strong spatial agreement with HEC-RAS, with IoU values ranging from 0.631 to 0.790 in 2019 and 0.737 to 0.768 in 2024. F1-scores remain consistently above 0.77 and exceed 0.85 during peak stages in both events.

 doi:10.20944/preprints202603.2381.v1

Table 4. Stage-specific spatial performance of the LSTM–U-Net model.

Year	Date	IoU	F1-score	Kappa
2019	8/21/2019	0.631	0.774	0.744
	9/1/2019	0.790	0.883	0.853
	9/11/2019	0.781	0.877	0.852
2024	9/10/2024	0.737	0.848	0.824
	9/24/2024	0.753	0.859	0.825
	10/2/2024	0.768	0.868	0.844

For the 2019 event, the early stage on 21 August (HEC-RAS inundation area = 25.78 km²) shows moderate agreement (IoU = 0.631; F1 = 0.774), with slight overestimation along expanding flood margins (Figure 8). Spatial agreement improves during the peak stage on 01 September (54.95 km²) (IoU = 0.790; F1 = 0.883), where the predicted inundation pattern closely matches the core floodplain structure simulated by HEC-RAS. During the late stage on 11 September (47.24 km²), agreement remains high (IoU = 0.781; F1 = 0.877), with deviations largely confined to shallow peripheral zones.

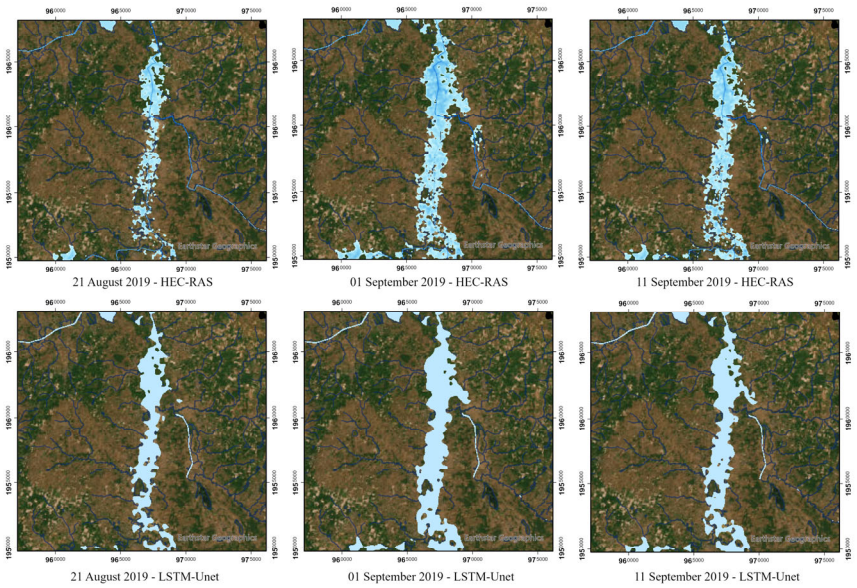

Figure 8. Spatial comparison of HEC-RAS and LSTM–U-Net model for the 2019 flood event.

A similar pattern is observed for the 2024 event. During the early stage on 10 September (34.05 km²), agreement remains high (IoU = 0.737; F1 = 0.848), with minor discrepancies near transitional flood boundaries (Figure 9). At the mid-stage on 24 September (51.01 km²), the hybrid model captures the overall inundation pattern well (IoU = 0.753; F1 = 0.859), including lateral expansion along the central floodplain. The late stage on 02 October (38.07 km²) also shows strong spatial agreement (IoU = 0.768; F1 = 0.868), indicating consistent performance throughout flood recession. Across all stages, the inundation core remains spatially consistent, with no clear fragmentation or displacement.

 doi:10.20944/preprints202603.2381.v1

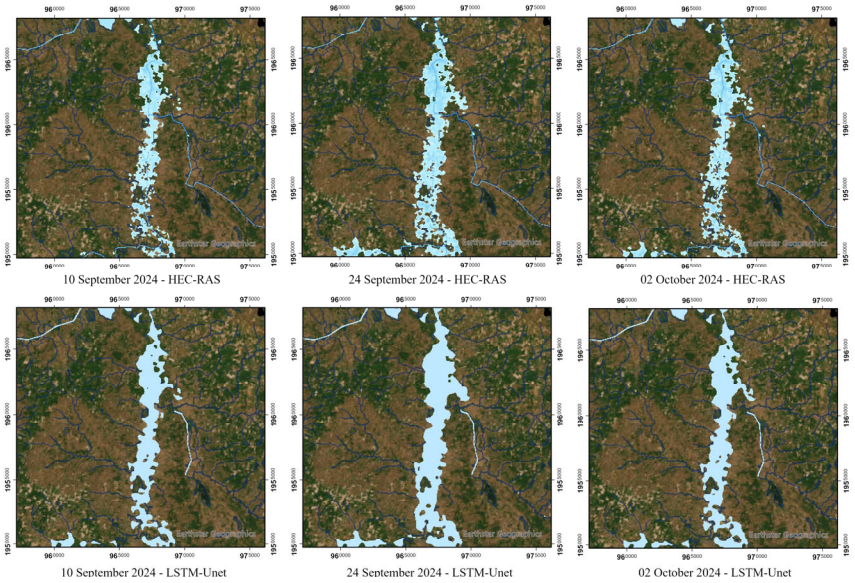

Figure 9. Spatial comparison of HEC-RAS and LSTM–U-Net model for the 2024 flood event.

The error pattern further helps explain model behavior (Figure 10; Table 5). Overprediction is most pronounced during early-stage expansion, particularly in 2019 (27.7%), whereas underprediction remains comparatively low (<6% in all cases). Error maps show that discrepancies are concentrated along shallow floodplain boundaries rather than within the central inundation zone. This pattern suggests that most errors are related to threshold effects during flood expansion and recession, rather than to systematic omission of peak inundation areas.

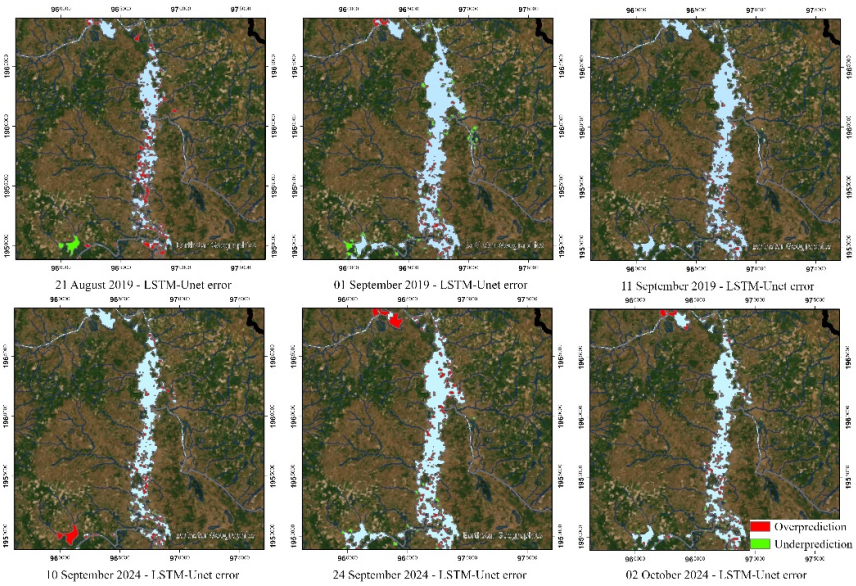

Figure 10. Spatial distribution of overprediction and underprediction for the 2019 and 2024 validation events.

Table 5. Quantitative error metrics of the LSTM–U-Net model compared with HEC-RAS.

Year	Date	Overprediction (km²)	Overprediction (%)	Underprediction (km²)	Underprediction (%)
2019	8/21/2019	7.14	27.71	0.73	2.83
	9/1/2019	3.87	7.04	3.03	5.51

 doi:10.20944/preprints202603.2381.v1

	9/11/2019	4.3	9.1	1.65	3.5
	9/10/2024	5.14	15.09	1.02	2.99
2024	9/24/2024	6.6	12.93	1.41	2.76
	10/2/2024	4.55	11.95	1.5	3.93

3.3. Climate Change Impact and Future Flood Inundation Projection

3.3.1. Climate-Driven Changes in Monthly Runoff

Projected monthly discharge under SSP2-4.5 and SSP5-8.5 shows pronounced seasonal concentration, with most runoff occurring during July–October (Figure 11). During the flood season, discharge exceeds the historical 30-year mean (60–150 m³/s), with August–September increases of approximately 30–90%, indicating intensified flood-generating conditions.

Under SSP2-4.5, the near-term projection (2029) exhibits the highest flood-season discharge, with August–September values of 160–165 m³/s (20–40% above historical levels), while mid- and late-term periods (2034 and 2044) show more moderate increases of 10–30%. In contrast, SSP5-8.5 demonstrates stronger intensification, particularly in the mid- and late-term projections, with peak monthly discharge frequently exceeding 200 m³/s and reaching 230–235 m³/s (50–80% above historical conditions). Both scenarios also indicate increased inter-month variability and earlier wet-season discharge (May–June).

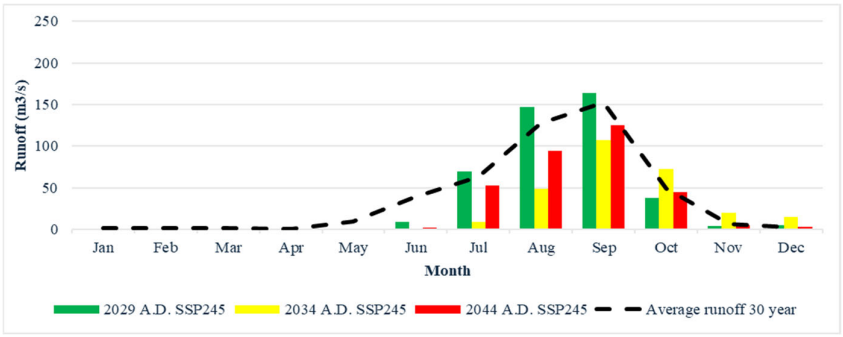

(**a**)

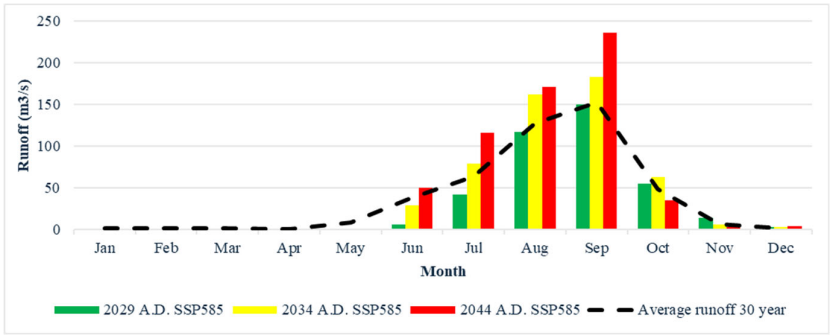

(**b**)

Figure 11. Monthly mean discharge projections under SSP2-4.5 (a) and SSP5-8.5 (b) for selected future years, compared with the historical 30-year average.

 doi:10.20944/preprints202603.2381.v1

3.3.2. Event-Based Changes in Future Flood Inundation Extent

Event-based analysis of the maximum annual inundation maps shows different temporal patterns under the two emission scenarios (Figure 12). Under SSP2-4.5, the largest simulated flood extent occurs in 2029, reaching 64.06 km². The maximum inundation area decreases to 50.85 km² in 2034 (−21% relative to 2029) and further declines to 47.31 km² in 2044 (−26%), indicating no consistent increasing trend across the projected periods.

In contrast, SSP5-8.5 shows a progressive increase in maximum annual flood extent, expanding from 57.77 km² in 2029 to 62.60 km² in 2034 (+8%) and 69.91 km² in 2044 (+21%). However, the increase in inundation extent remains smaller than the projected increase in peak discharge, suggesting a nonlinear floodplain response.

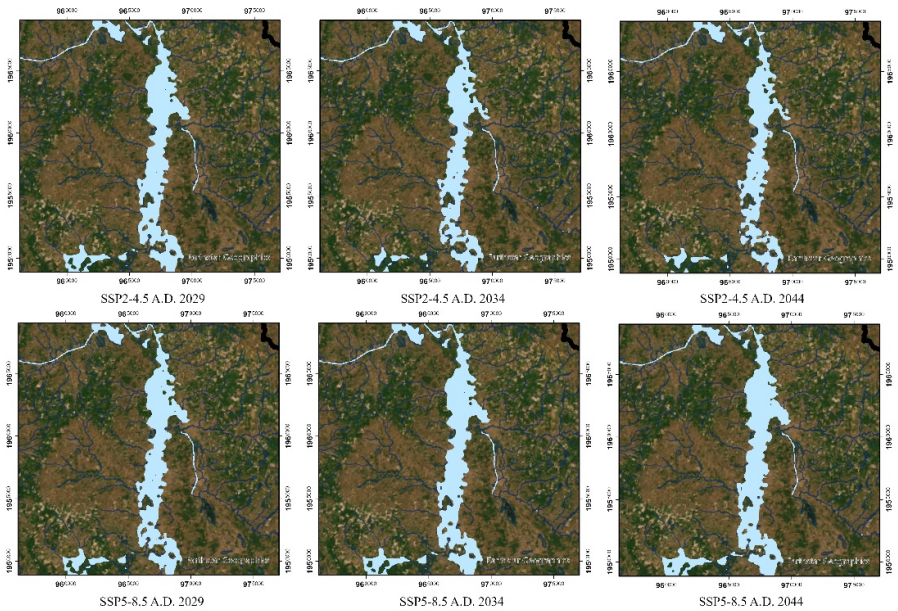

Figure 12. Future flood inundation under SSP2-4.5 and SSP5-8.5 scenarios for 2029, 2034, and 2044.

4. Discussion

4.1. Representation of Flood Processes Using Coupled Model

The strong hydrological (NSE = 0.896; KGE = 0.827) and hydraulic (F1 = 0.876; Kappa = 0.873) performance indicates that the coupled HEC-HMS–HEC-RAS framework provides a reliable and physically consistent basis for flood simulation in the Upper Songkhram Basin. The framework captures both runoff generation and downstream floodplain response within the same modelling chain. This is consistent with previous applications in low-gradient, monsoon-influenced floodplains [10,53,54]. It is also supported by Peker *et al.* (2024) [10], who showed that coupling hydrological and hydraulic models improves the representation of both discharge and inundation dynamics. In the Upper Songkhram Basin, flooding is controlled not only by runoff magnitude but also by channel–floodplain interactions and basin-scale storage processes [27], indicating a storage-influenced flood regime. This behavior is further shaped by the basin's geomorphological characteristics, including low relief, gentle slope, elongated basin form, and strong lateral connectivity (Table 1), which promote overbank flow, temporary storage, and attenuation of flood wave propagation [4].

Under these conditions, a single-model approach would represent only part of the flood system and could misrepresent the relationship between discharge and inundation extent. In low-gradient floodplains, part of the incoming discharge is temporarily stored and later released, while flow is redistributed across the floodplain. Wohl (2021) [55] emphasized that floodplains function as

 doi:10.20944/preprints202603.2381.v1

dynamic storage systems, where temporary storage and delayed release can weaken the direct relationship between discharge magnitude and inundation extent. As a result, similar discharge magnitudes may produce different inundation extents depending on antecedent storage conditions. Therefore, a coupled modelling approach is needed to represent both basin-scale hydrological processes and downstream floodplain dynamics.

4.2. Efficient Surrogate Modeling Using Hybrid Deep Learning

The comparison between the two-dimensional HEC-RAS simulations and the LSTM–U-Net model highlights the complementary roles of physics-based hydraulics and deep learning surrogates. HEC-RAS explicitly simulates floodplain hydraulics in low-gradient basins, while the LSTM–U-Net model captures the dominant inundation structure, particularly in the spatial organization of core flooded areas [12,14]. This suggests that the surrogate model preserves the primary spatial response of the hydraulic system rather than simply estimating flood extent. This spatial consistency is also reflected in the temporal domain, where the model maintains stable agreement with observed inundation patterns across different flood periods (Figure 13). Validation results in Section 3.2.2 further confirm that the hybrid framework reproduces the main inundation dynamics of the study floodplain while preserving this dominant spatial response. The lag-length sensitivity reported in Section 3.2.1 further suggests that inundation in the Upper Songkhram Basin depends not only on topography and floodplain storage, but also on antecedent hydrological conditions. This is consistent with the role of short-term hydrological memory in low-gradient, storage-dominated floodplains, where inundation extent is influenced by cumulative filling and antecedent system state rather than by discharge at a single time step [11,17].

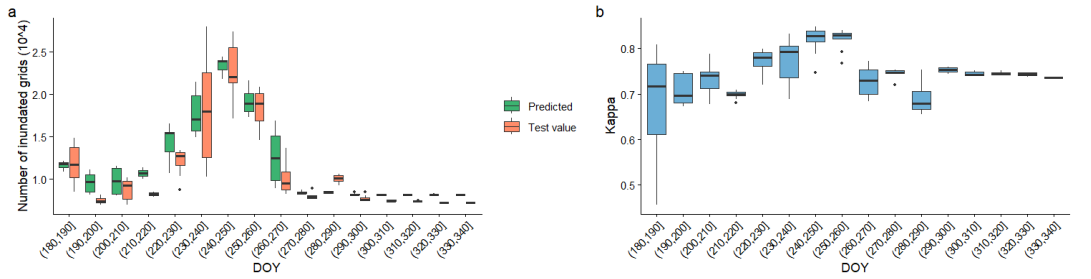

(a)

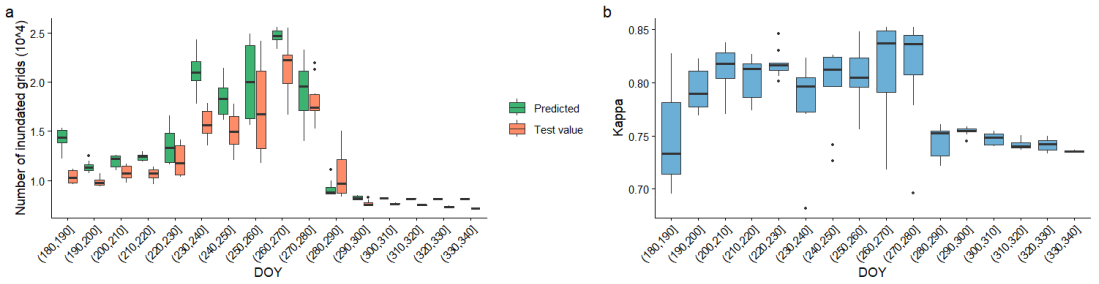

(b)

Figure 13. Temporal validation of the LSTM–U-Net model for the flood events: (a) 2019 and (b) 2024.

While the LSTM-U-Net model captures the main inundation pattern, especially in the floodplain core, the spatial distribution of error helps explain model behavior. As shown in Section 3.2.3, most discrepancies occur along shallow inundation boundaries, whereas the floodplain core remains consistent with HEC-RAS. This pattern is consistent with Li *et al.* (2025) [56], who reported boundary delineation errors in complex floodplains, and Noori *et al.* (2025) [57], who found classification

 doi:10.20944/preprints202603.2381.v1

uncertainty in transition zones and shallow flooded areas. These discrepancies likely reflect the sensitivity of shallow floodplain edges to threshold-based flood classification, where small changes in water level can shift pixels between flooded and non-flooded states [51]. Such uncertainty is common in transition zones and may be increased by heterogeneous land cover and human alteration [58,59]. Despite these uncertainties, the model captures large-scale inundation patterns well, showing the value of deep learning as a surrogate for hydraulic simulations.

4.3. Future Flood Regime Shifts in the Upper Songkhram Basin

The coupled hydrological and inundation projections indicate a future shift in the flood regime of the Upper Songkhram Basin. Under CMIP6 SSP2-4.5 and SSP5-8.5, wet-season discharge increases markedly, whereas maximum inundation extent expands more moderately (Sections 3.3.1 and 3.3.2). This indicates a nonlinear relationship between discharge and flood extent [60] and reflects a storage-dominated floodplain response. This response is consistent with the basin's geomorphological setting, where low relief, broad floodplain storage, and strong lateral connectivity limit the proportional expansion of flooding [4]. As a result, larger increases in discharge do not necessarily lead to equally large increases in inundation extent.

Scenario differences also follow this pattern. The weaker and more variable response under SSP2-4.5 may reflect the stronger influence of regional climate variability and relatively moderate warming, leading to spatially and temporally inconsistent precipitation changes [61]. This interpretation is consistent with the findings of Hormwichian *et al*. (2023) [62], who showed that changes under SSP2-4.5 in the Upper Chi Basin, northeastern Thailand, remained relatively close to baseline conditions, whereas SSP5-8.5 showed a clearer increase in wet-season runoff, especially toward the late century. A similar finding was reported by Try *et al.* (2024) [63], who found that high-emission scenarios over Southeast Asia are associated with stronger increases in climate extremes, including heavy precipitation. Together, these findings suggest a shift toward more persistent and potentially more severe flood conditions under high-emission scenarios.

5. Conclusions

This study developed a hybrid modelling framework that integrates a coupled hydrological–hydraulic model with a deep learning–based flood inundation model to simulate flood dynamics in the Upper Songkhram River Basin. By combining the physically based HEC-HMS and HEC-RAS models with a data-driven LSTM–U-Net architecture, the framework preserves the linkage between runoff generation and floodplain response while supporting scenario-based simulations. The strong performance of both the hydrological component (NSE = 0.896; KGE = 0.827; R^2 = 0.909) and the hydraulic component (F1 = 0.876; Kappa = 0.873) indicates that the coupled system provides a physically consistent basis for generating reliable training data for the surrogate model.

The LSTM–U-Net model reproduced the main inundation patterns across independent flood events, achieving a mean F1-score of 0.838 and IoU of 0.721 relative to HEC-RAS simulations. Model performance remained stable across different flood stages, with most discrepancies occurring along shallow floodplain margins. This indicates that the surrogate captures the core inundation structure well, although some uncertainty remains along threshold-sensitive boundaries. These results suggest that physics-constrained surrogates can provide an effective alternative to fully hydraulic simulations while preserving the main spatial characteristics of flood behavior.

Application of the hybrid framework to CMIP6 climate scenarios indicates a future shift in the flood regime of the Upper Songkhram Basin, with a nonlinear relationship between discharge and inundation extent. While SSP2-4.5 shows weaker and more variable changes, SSP5-8.5 shows a clearer increase in flood extent, reaching about 21% by 2044 relative to 2029. More importantly, the results indicate that larger increases in discharge do not necessarily lead to equally large increases in inundation extent, reflecting the storage-dominated behavior of the floodplain system. This implies that flood hazard may intensify even when changes in inundation extent remain moderate, highlighting the need to consider nonlinear floodplain response in future risk assessments.

 doi:10.20944/preprints202603.2381.v1

Funding: This research received no external funding.

Author Contributions: Conceptualization, methodology, analysis, investigation, visualization, and writing—original draft, T.N.; supervision, review, and editing, P.T. and N.K. All authors have read and agreed to the published version of the manuscript.

Data Availability Statement: The datasets, including technical and observational data, generated and/or analyzed during this study are available from the corresponding author upon reasonable request.

Conflicts of Interest: The authors declare no conflicts of interest.

Acknowledgments: During the preparation of this manuscript, the authors used ChatGPT (OpenAI) and Perplexity for idea exploration, conceptual development, and identification of potential research gaps. The tools were not used to generate data, perform analyses, or derive scientific conclusions. The authors reviewed and edited the output and take full responsibility for the content of this publication.

References

1. Intergovernmental Panel on Climate Change. *Climate Change 2021*: *The Physical Science Basis*. Contribution of Working Group I to the Sixth Assessment Report of the Intergovernmental Panel on Climate Change; Cambridge University Press: Cambridge, UK, 2021. https://doi.org/10.1017/9781009157896.
2. Blöschl, G.; Hall, J.; Viglione, A.; Perdigão, R.A.P.; Parajka, J.; Merz, B.; Lun, D.; Arheimer, B.; Aronica, G.T.; Bilibashi, A.; et al. Changing climate both increases and decreases European river floods. *Nature* 2019, 573, 108-111. https://doi.org/10.1038/s41586-019-1495-6.
3. Nardi, F.; Vivoni, E.R.; Grimaldi, S. Investigating a floodplain scaling relation using a hydrogeomorphic delineation method. *Water Resour. Res*. 2006, 42, W09409. https://doi.org/10.1029/2005WR004155.
4. Farrag, M.; Brill, F.; Dung, N.V.; Sairam, N.; Schröter, K.; Kreibich, H.; Merz, B.; de Bruijn, K.M.; Vorogushyn, S. On the role of floodplain storage and hydrodynamic interactions in flood risk estimation. *Hydrol. Sci. J.* 2022, 67, 508–534. https://doi.org/10.1080/02626667.2022.2030058.
5. Fleischmann, A.S.; Paiva, R.C.D.; Collischonn, W.; Sorribas, M.V.; Pontes, P.R.M. On river-floodplain interaction and hydrograph skewness. *Water Resour. Res.* 2016, 52, 7615–7630. https://doi.org/10.1002/2016WR019233.
6. Tull, N.; Passalacqua, P. Flood Wave Attenuation as a Function of Floodplain Storage, Secondary Channel Conveyance, and Discharge. *Water Resour. Res.* 2025, 61, e2024WR038582. https://doi.org/10.1029/2024WR038582.
7. Teng, J.; Jakeman, A.J.; Vaze, J.; Croke, B.F.W.; Dutta, D.; Kim, S. Flood inundation modelling: A review of methods, recent advances and uncertainty analysis. *Environ. Model. Softw.* 2017, 90, 201–216. https://doi.org/10.1016/j.envsoft.2017.01.006.
8. Bates, P.D.; De Roo, A.P.J. A simple raster-based model for flood inundation simulation. *J. Hydrol.* 2000, 236, 54–77. https://doi.org/10.1016/S0022-1694(00)00278-X.
9. Neal, J.; Schumann, G.; Bates, P. A subgrid channel model for simulating river hydraulics and floodplain inundation over large and data sparse areas. *Water Resour. Res.* 2012, 48, W11506. https://doi.org/10.1029/2012WR012514.
10. Peker, İ.B.; Gülbaz, S.; Demir, V.; Orhan, O.; Beden, N. Integration of HEC-RAS and HEC-HMS with GIS in flood modeling and flood hazard mapping. *Sustainability* 2024, 16, 1226. https://doi.org/10.3390/su16031226.
11. Pathiraja, S.; Westra, S.; Sharma, A. Why continuous simulation? The role of antecedent moisture in design flood estimation. *Water Resour. Res.* 2012, 48, W06534. https://doi.org/10.1029/2011WR010997.
12. Haces-García, F.; Ross, N.; Glennie, C.L.; Rifai, H.S.; Hoskere, V.; Ekhtari, N. Rapid 2D hydrodynamic flood modeling using deep learning surrogates. *J. Hydrol.* 2025, 651, 132561. https://doi.org/10.1016/j.jhydrol.2024.132561.
13. Kabir, S.R.; Patidar, S.; Xia, X.; Liang, Q.; Neal, J.; Pender, G. A deep convolutional neural network model for rapid prediction of fluvial flood inundation. J. *Hydrol.* 2020, 590, 125481. https://doi.org/10.1016/j.jhydrol.2020.125481.

 doi:10.20944/preprints202603.2381.v1

14. Zhou, Y.; Guo, S.; Chang, F.-J.; Liu, P.; Chen, A. Deep Learning-Based Rapid Flood Inundation Modeling for Flat Floodplains With Complex Flow Paths. *Water Resour. Res.* 2022, 58, e2022WR033214. https://doi.org/10.1029/2022WR033214.
15. Frahér, N.; Wang, Q.J.; Wu, W.; Nathan, R. Assessment of surrogate models for flood inundation: The physics-guided LSG model vs. state-of-the-art machine learning models. *Water Res.* 2024, 252, 121202. https://doi.org/10.1016/j.watres.2024.121202.
16. Wasko, C.; Nathan, R.; Peel, M.C. Changes in antecedent soil moisture modulate flood seasonality in a changing climate. *Water Resour. Res.* 2020, 56, e2019WR026300. https://doi.org/10.1029/2019WR026300.
17. Staudinger, M.; Kauzlaric, M.; Mas, A.; Evin, G.; Hingray, B.; Viviroli, D. The role of antecedent conditions in translating precipitation events into extreme floods at the catchment scale and in a large-basin context. *Nat. Hazards Earth Syst. Sci.* 2025, 25, 247–265. https://doi.org/10.5194/nhess-25-247-2025.
18. Eyring, V.; Bony, S.; Meehl, G.A.; Senior, C.A.; Stevens, B.; Stouffer, R.J.; Taylor, K.E. Overview of the Coupled Model Intercomparison Project Phase 6 (CMIP6) experimental design and organization. *Geosci. Model Dev.* 2016, 9, 1937–1958. https://doi.org/10.5194/gmd-9-1937-2016.
19. Mosimann, M.; Kauzlaric, M.; Schick, S.; Martius, O.; Zischg, A.P. Evaluation of surrogate flood models for the use in impact-based flood warning systems at national scale. *Environ. Model. Softw.* 2024, 173, 105936. https://doi.org/10.1016/j.envsoft.2023.105936.
20. Yang, F.; Ding, W.; Zhao, J.; Song, L.; Yang, D.; Li, X. Rapid urban flood inundation forecasting using a physics-informed deep learning approach. *J. Hydrol.* 2024, *643*, 131998. https://doi.org/10.1016/j.jhydrol.2024.131998.
21. Woo, H.; Choi, H.; Kim, M.; Noh, S.J. Physics-guided deep learning for spatiotemporal evolution of urban pluvial flooding. *Water* 2025, *17*, 1239. https://doi.org/10.3390/w17081239.
22. Donnelly, J.; Daneshkhah, A.; Abolfathi, S. Physics-informed neural networks as surrogate models of hydrodynamic simulators. *Sci. Total Environ.* 2024, 912, 168814. https://doi.org/10.1016/j.scitotenv.2023.168814.
23. Shrestha, S.; Bhatta, B.; Shrestha, M.; Shrestha, P.K. Integrated assessment of the climate and land-use change impact on hydrology and water quality in the Songkhram River Basin, Thailand. *Sci. Total Environ.* 2018, 643, 1610-1622. https://doi.org/10.1016/j.scitotenv.2018.06.306.
24. Hydro and Agro Informatics Institute (HAII). *Data Collection and Analysis for the Development of a Data Warehouse System for 25 River Basins and Flood–Drought Simulation Models: Mekong River Basin* [in Thai]; HAII: Bangkok, Thailand, 2012. Available online: https://tiwrm.hii.or.th/web/attachments/25basins/02-khong.pdf
25. ASF DAAC. ALOS PALSAR High Resolution Radiometric Terrain Corrected Product [data set]; NASA Alaska Satellite Facility Distributed Active Archive Center, 2014. https://doi.org/10.5067/Z97HFCNKR6VA.
26. Sakon Nakhon Provincial Integrated Administration Committee. Sakon Nakhon Provincial Development Plan (5-Year Plan: 2023–2027), Fiscal Year 2023 Edition; Sakon Nakhon Province: Sakon Nakhon, Thailand, 2024.
27. Walalite, T.; Dekker, S.C.; Keizer, F.M.; Kardel, I.; Schot, P.P.; de Jong, S.M.; Wassen, M.J. Flood water hydrochemistry patterns suggest floodplain sink function for dissolved solids from the Songkhram monsoon river (Thailand). *Wetlands* 2016, 36, 995–1008. https://doi.org/10.1007/s13157-016-0814-z.
28. Bangkok Post. Sonca Storm Wrath Sinks Sakon Nakhon, 29 July 2017. Available online: https://www.bangkokpost.com/thailand/general/1295847/sonca-storm-wrath-sinks-sakon-nakhon.
29. Feldman, A.D., Ed. Hydrologic Modeling System HEC-HMS: Technical Reference Manual; U.S. Army Corps of Engineers, *Hydrologic Engineering Center*: Davis, CA, USA, 2000.
30. U.S. Army Corps of Engineers, Hydrologic Engineering Center. *HEC-HMS Hydrologic Modeling System User's Manual*, Version 4.3; U.S. Army Corps of Engineers: Davis, CA, USA, 2018. Available online: https://www.hec.usace.army.mil/software/hec-hms/documentation/HEC-HMS_Users_Manual_4.3.pdf
31. U.S. Department of Agriculture, Soil Conservation Service. *National Engineering Handbook, Section 4: Hydrology, Chapter 21: Design Hydrographs*; U.S. Department of Agriculture: Washington, DC, USA, 1972. Available online: https://irrigationtoolbox.com/NEH/Part%20630%20Hydrology/neh630-ch21.pdf
32. Mishra, S.K.; Singh, V.P. Soil Conservation Service Curve Number (SCS-CN) Methodology; *Springer: Dordrecht*, The Netherlands, 2003. https://doi.org/10.1007/978-94-017-0147-1.

 doi:10.20944/preprints202603.2381.v1

33. Snyder, F.F. Synthetic unit-graphs. *Eos Trans. Am. Geophys. Union* 1938, 19, 447–454. https://doi.org/10.1029/TR019i001p00447.
34. Chow, V.T.; Maidment, D.R.; Mays, L.W. Applied Hydrology; McGraw-Hill: New York, NY, USA, 1988.
35. McCarthy, G.T. The unit hydrograph and flood routing. In Proceedings of the Conference of North Atlantic Division, U.S. Army Corps of Engineers, New London, CT, USA, 24 June 1938; pp. 608–609.
36. Chow, V.T. Open-Channel Hydraulics; McGraw-Hill: New York, NY, USA, 1959.
37. U.S. Army Corps of Engineers. *HEC-RAS River Analysis System: User's Manual, Version 5.0*; Hydrologic Engineering Center: Davis, CA, USA, 2016.
38. Vashist, K.V.; Singh, K.K. HEC-RAS 2D modeling for flood inundation mapping: A case study of the Krishna River Basin. *Water Pract. Technol.* 2023, 18, 831–844. https://doi.org/10.2166/wpt.2023.048.
39. El-Haddad, B.; Youssef, A.M.; Pourghasemi, H.R.; El-Kholy, A.; Mohamed, A.A.; Arabameri, A. Flood inundation mapping using HEC-RAS 2D modeling and examining the impact of changes in the model-meshing pixel scale on the final output. *Water Resour. Manag.* 2025, 39, 3811–3830. https://doi.org/10.1007/s11269-025-04228-0.
40. Zahura, F.T.; Goodall, J.L.; Sadler, J.M.; Shen, Y.; Morsy, M.M.; Behl, M.; Bowes, B.D. Training Machine Learning Surrogate Models From a High-Fidelity Physics-Based Model: Application for Real-Time Street-Scale Flood Prediction in an Urban Coastal Community. *Water Resources Research* 2020, 56, e2019WR027038. https://doi.org/10.1029/2019WR027038.
41. Hochreiter, S.; Schmidhuber, J. Long short-term memory. *Neural Comput.* 1997, 9, 1735–1780. https://doi.org/10.1162/neco.1997.9.8.1735.
42. Ronneberger, O.; Fischer, P.; Brox, T. U-Net: Convolutional Networks for Biomedical Image Segmentation. In *Medical Image Computing and Computer-Assisted Intervention—MICCAI 2015*; Navab, N.; Hornegger, J.; Wells, W.M.; Frangi, A.F., Eds.; Lecture Notes in Computer Science; Springer: Cham, Switzerland, 2015; Volume 9351, pp. 234–241. https://doi.org/10.1007/978-3-319-24574-4_28.
43. Caruana, R. Multitask learning. *Mach. Learn*. 1997, 28, 41–75. https://doi.org/10.1023/A:1007379606734.
44. Milletari, F.; Navab, N.; Ahmadi, S.-A. V-Net: Fully Convolutional Neural Networks for Volumetric Medical Image Segmentation. In Proceedings of the 2016 Fourth International Conference on 3D Vision (3DV); 2016; pp. 565–571. https://doi.org/10.1109/3DV.2016.79.
45. Cannon, A.J.; Sobie, S.R.; Murdock, T.Q. Bias correction of GCM precipitation by quantile mapping: How well do methods preserve changes in quantiles and extremes? *J. Clim*. 2015, 28, 6938-6959. https://doi.org/10.1175/JCLI-D-14-00754.1.
46. Taylor, K.E. Summarizing model performance in a single diagram. *J. Geophys. Res. Atmos.* 2001, 106, 7183–7192. https://doi.org/10.1029/2000JD900719.
47. Nash, J.E.; Sutcliffe, J.V. River flow forecasting through conceptual models part I—A discussion of principles. *J. Hydrol.* 1970, 10, 282–290. https://doi.org/10.1016/0022-1694(70)90255-6.
48. Gupta, H.V.; Kling, H.; Yilmaz, K.K.; Martinez, G.F. Decomposition of the mean squared error and NSE performance criteria: Implications for improving hydrological modelling. *J. Hydrol.* 2009, 377, 80–91. https://doi.org/10.1016/j.jhydrol.2009.08.003.
49. Moriasi, D.N.; Arnold, J.G.; Van Liew, M.W.; Bingner, R.L.; Harmel, R.D.; Veith, T.L. Model evaluation guidelines for systematic quantification of accuracy in watershed simulations. *Trans. ASABE* 2007, 50, 885–900. https://doi.org/10.13031/2013.23153.
50. Powers, D.M.W. Evaluation: From precision, recall and F-measure to ROC, informedness, markedness and correlation. *J. Mach. Learn. Technol.* 2011, 2, 37–63.
51. Stephens, E.M.; Schumann, G.J.-P.; Bates, P.D. Problems with binary pattern measures for flood model evaluation. Hydrol. Process. 2014, 28, 4928–4937. https://doi.org/10.1002/hyp.9979.
52. Wing, O.E.J.; Bates, P.D.; Smith, A.M.; Sampson, C.C.; Johnson, K.A.; Erickson, T.A. Validation of a 30 m resolution flood hazard model of the conterminous United States. *Water Resour. Res.* 2017, 53, 7968–7986. https://doi.org/10.1002/2017WR020917.
53. Hdeib, R.; Abdallah, C.; Colin, F.; Brocca, L.; Moussa, R. Constraining coupled hydrological-hydraulic flood model by past storm events and post-event measurements in data-sparse regions. *J. Hydrol.* 2018, 565, 160–175. https://doi.org/10.1016/j.jhydrol.2018.08.008.

 doi:10.20944/preprints202603.2381.v1

54. Thakur, B.; Parajuli, R.; Kalra, A.; Ahmad, S.; Gupta, R. Coupling HEC-RAS and HEC-HMS in Precipitation Runoff Modelling and Evaluating Flood Plain Inundation Map. In World Environmental and Water Resources Congress 2017; Sacramento, CA, USA, 21–25 May 2017; pp. 240–251. https://doi.org/10.1061/9780784480625.022.
55. Wohl, E. An integrative conceptualization of floodplain storage. *Rev. Geophys*. 2021, 59, e2020RG000724. https://doi.org/10.1029/2020RG000724.
56. Li, L.; Zhao, Y.; Qin, S.; Pan, D.; Zhang, J.; Li, A.; Hu, Q. PhysWRNet: A physics-guided deep learning framework for flood inundation mapping with SAR and hydrodynamic simulations. *J. Hydrol.* 2026, 665, 134662. https://doi.org/10.1016/j.jhydrol.2025.134662.
57. Noori, A.M.; Ziboon, A.R.T.; Al-Hameedawi, A.N. Deep-learning integration of CNN-Transformer and U-Net for bi-temporal SAR flash-flood detection. *Appl. Sci.* 2025, 15, 7770. https://doi.org/10.3390/app15147770.
58. Aristizabal, F.; Judge, J.; Monsivais-Huertero, A. High-resolution inundation mapping for heterogeneous land covers with synthetic aperture radar and terrain data. *Remote Sens*. 2020, 12, 900. https://doi.org/10.3390/rs12060900.
59. Rajib, A.; Zheng, Q.; Lane, C.R.; Golden, H.E.; Christensen, J.R. Human alterations of the global floodplains 1992–2019. *Sci. Data* 2023, 10, 499. https://doi.org/10.1038/s41597-023-02382-x.
60. Shukla, T.; Salas, C.R.; Pankau, R.C.; Rhoads, B.L. Critical linkages among floodplain hydrology, geomorphology and ecology along a lowland meandering river, Illinois, USA. *Ecohydrology* 2024, 17, e2661. https://doi.org/10.1002/eco.2661.
61. Singh, V.; Qin, X. Study of rainfall variabilities in Southeast Asia using long-term gridded rainfall and its substantiation through global climate indices. *J. Hydrol*. 2020, 585, 124320. https://doi.org/10.1016/j.jhydrol.2019.124320.
62. Hormwichian, R.; Kaewplang, S.; Kangrang, A.; Supakosol, J.; Boonrawd, K.; Sriworamat, K.; Muangthong, S.; Songsaengrit, S.; Prasanchum, H. Understanding the interactions of climate and land use changes with runoff components in spatial-temporal dimensions in the Upper Chi Basin, Thailand. *Water* 2023, 15, 3345. https://doi.org/10.3390/w15193345.
63. Try, S.; Qin, X. Evaluation of future changes in climate extremes over Southeast Asia using downscaled CMIP6 GCM projections. *Water* 2024, 16, 2207. https://doi.org/10.3390/w16152207.